ADVANCED FUNCTIONAL MATERIALS
www.afm-journal.de

Anion-Regulated Electric Double Layer and Progressive Nucleation Enable Uniform and Nanoscale Zn Deposition for Aqueous Zinc-Ion Batteries

*Ziqing Wang, Jiefeng Diao, Graeme Henkelman, and C. Buddie Mullins**

Aqueous zinc-ion batteries have been regarded as safe and cheap energy storage devices. However, severe zinc dendrite growth and water decomposition limit the sustainability of aqueous zinc-ion batteries. Herein, sodium-difluoro(oxalato)borate (NaDFOB) is introduced into $ZnSO_4$ electrolyte to modify the electric double layer (EDL) and the nucleation mechanism. Electrochemical tests and density functional theory calculations reveal that $DFOB^-$ adsorbs on the zinc electrode to form a water-poor EDL, effectively suppressing side reactions. Notably, a detailed investigation of zinc deposition demonstrates that the adsorbed $DFOB^-$ ions induce progressive nucleation, resulting in nanoscale zinc nuclei and uniform zinc growth. Additionally, the adsorbed $DFOB^-$ ions decompose into a solid electrolyte interphase, further protecting the zinc electrode. Consequently, the Zn/Zn symmetric cell using $ZnSO_4$/NaDFOB electrolyte can cycle for over 500 h at 5 mA cm^{-2} to reach a capacity of 10 mAh cm^{-2}, while a Zn/Cu half cell maintains an average Coulombic efficiency of 99.3% over 400 cycles. A high capacity retention of 93.0% with a capacity of 250 mAh g^{-1} at 0.2 A g^{-1} is achieved in the $ZnSO_4$/NaDFOB electrolyte in full cell cycling. These findings highlight the impact of anion-modified EDL and progressive nucleation on achieving highly uniform zinc deposition.

1. Introduction

Aqueous zinc-ion batteries (AZIBs) have been developed as a safer and cheaper substitution for lithium-ion batteries due to their high theoretical capacity (820 mAh g^{-1}) and the non-flammability of aqueous electrolytes.[1–5] However, dendrite formation and parasitic reactions (i.e., byproducts, hydrogen evolution reaction (HER), and oxygen evolution reaction (OER)) negatively impact the Zn plating/stripping behavior and reduce the reversibility and stability of AZIBs.[6–12]

The properties of the electrolyte-electrode interface determine the Zn^{2+} desolvation process and Zn deposition behavior, thereby influencing the stability of the electrode.[13–17] Recently, multiple methods for modifying the electrode surface, including coating protective layers,[18–21] changing Zn anode structures,[22–25] and designing novel separators,[26–29] have been reported to mitigate parasitic reactions. However, despite the valuable insights into electrode protection from these methods, the complex fabrication and associated high cost have limited their further development. In contrast to these approaches, a more straightforward strategy has emerged via electrolyte optimization with different additives to modify the Zn electrode surface.[30–35] Due to the adsorption and decomposition of additives on the Zn electrode, the preferential exposure of certain crystalline facets (i.e., (002) and (100)), coupled with the in situ formation of the solid electrolyte interphase (SEI) layer has been demonstrated to improve the electrochemical performance of AZIBs.[30,31,36–40] Therefore, reorganizing the chemical environment on the electrolyte-electrode interface via modulating electrolyte components provides a potential approach for uniform Zn deposition and restricts undesirable reactions.

The electric double layer (EDL), which is the structure on the electrode surface comprising solvent molecules and ions, can notably influence the electrochemical reactions at the electrolyte-electrode interface.[41–43] The EDL was initially proposed by Helmholtz, and Graham introduced the notion of inner Helmholtz plane (IHP) and outer Helmholtz plane (OHP).[44,45] According to the Bockris-Devanathan-Müller model, the IHP for AZIBs accommodates water molecules and anions with specific adsorption tendencies, while the OHP consists of the solvated Zn^{2+} ions (Figure S1, Supporting Information).[46–48] This arrangement of water dipoles and ions within the EDL

Z. Wang, J. Diao, G. Henkelman, C. B. Mullins
Department of Chemistry
The University of Texas at Austin
Austin, TX 78712, United States
E-mail: mullins@che.utexas.edu
J. Diao, G. Henkelman
Oden Institute for Computational Engineering and Sciences
The University of Texas at Austin
Austin, TX 78712, United States
C. B. Mullins
McKetta Department of Chemical Engineering
The University of Texas at Austin
Austin, TX 78712, United States
C. B. Mullins
Texas Materials Institute and Center for Electrochemistry
The University of Texas at Austin
Austin, TX 78712, United States
The ORCID identification number(s) for the author(s) of this article can be found under https://doi.org/10.1002/adfm.202314002

DOI: 10.1002/adfm.202314002

results in direct interactions between water from the IHP and the Zn electrode.[49,50] Consequently, undesired side reactions, particularly the HER, inevitably occur on the electrode surface. The remaining OH^- from water decomposition subsequently reacts with anions in the IHP, culminating in zinc hydroxide byproducts (e.g., $Zn_4(OH)_6(SO_4)\cdot xH_2O$).[51] To alleviate the impact of these side reactions, a promising avenue involves reducing water content within the IHP. Therefore, modifying the IHP by introducing other additives holds significant potential to enhance the electrochemical performance of AZIBs.

Gaining insight into the mechanism of Zn deposition holds significance for designing highly reversible Zn plating/stripping. However, relying solely on the morphology and state of the post-deposited Zn electrode only offers a limited understanding of the Zn growth dynamics.[52] Hence, a more in-depth comprehension of Zn plating behavior can be obtained by investigating the initial stages of Zn nucleation and subsequent Zn nuclei growth.[53–55] Uniform Zn nucleation and growth lay the foundation for favorable Zn plating behavior. In contrast, an uneven distribution of Zn nuclei and the accumulation of Zn on the pre-existing Zn nuclei lead to undesirable Zn dendrites.[56] Therefore, understanding the nucleation thermodynamics and deposition kinetics is necessary to unravel the impact of Zn nucleation and growth on the eventual deposition outcomes.

Herein, we present an approach to optimize electrolytes by incorporating small quantities of sodium difluoro(oxalato)borate (NaDFOB) into a conventional $ZnSO_4$ electrolyte, which induces nanoscale Zn nucleation and eventual super uniform Zn deposition. The experimental and theoretical evidence suggests that the NaDFOB molecules chemically adsorb on the Zn surface, elevating the driving force for nucleation and growth. Notably, introducing NaDFOB results in a transformation of the Zn nucleation dynamics from instantaneous to progressive, consequently creating small-grain Zn nuclei and a highly homogenous and reversible Zn plating process. Furthermore, the adsorption of NaDFOB contributes to a water-poor EDL at the electrode-electrolyte interface, suppressing water decomposition and mitigating parasitic reactions. The $DFOB^-$ ions in the EDL decompose and yield an SEI layer comprised of inorganic compounds, further inhibiting direct electrode-water contact. As a result, the Zn electrode immersed in the $ZnSO_4$/NaDFOB electrolyte exhibits favorable Zn plating/stripping reversibility with an average Coulombic efficiency (CE) of 99.3% over 400 cycles at 1 mA cm^{-2}. Due to the NaDFOB-induced progressive nucleation, Zn/Zn symmetric cells display prolonged cycling stability, enduring over 500 h at 0.5 and 5 mA cm^{-2} while achieving a capacity of 1 and 10 mAh cm^{-2}. Employing a $ZnSO_4$/NaDFOB electrolyte, the $Na_{0.33}V_2O_5$/Zn full cell battery maintains 93.0% of its capacity following 100 cycles at a current density of 0.2 A g^{-1}. This strategy, which regulates EDL on the electrolyte-electrode interface and promotes progressive nucleation with small nuclei, offers a promising avenue for developing dendrite-free Zn electrodes and highly stable aqueous zinc-ion batteries.

2. Results and Discussion

2.1. Characterization and Physicochemical Properties of Electrolytes

NaDFOB additives with gradient concentrations from 0.01 to 0.10 mol L^{-1} (M) were introduced into 2 M $ZnSO_4$ solution. As shown in Figure S2 (Supporting Information), the electrolytes with low concentrations of NaDFOB display clear solutions without any precipitation, while white solid precipitated from the electrolyte with 0.10 M NaDFOB due to the inferior solubility of NaDFOB in the aqueous solution. Further, the Zn deposition performance within the electrolytes with different NaDFOB concentrations demonstrates poor homogeneity under lower amounts of NaDFOB. Therefore, combining the above results, 2 M $ZnSO_4$ solution with 0.05 M NaDFOB additive (referred to as $ZnSO_4$/NaDFOB) was selected as the optimized electrolyte in this work. Characterization results of pure 2 M $ZnSO_4$ solution and $ZnSO_4$/NaDFOB indicate the chemical coordination of both solutions. Attenuated total reflectance-Fourier transform infrared (ATR-FTIR) and Raman spectra indicate that the NaDFOB molecules slightly break hydrogen bonds between water molecules and weaken the interactions between Zn^{2+} and SO_4^{2-} (Figures S3 and S4, Supporting Information).[31,57] The results of the density functional theory (DFT) molecular dynamic (MD) simulation confirm that the coordination environment and solvation structure of Zn^{2+} have been barely affected by the addition of NaDFOB (Figure S5, Supporting Information). The tiny influence of NaDFOB on the bulk electrolyte and solvation structure can be attributed to the small amount of NaDFOB in the electrolyte. To evaluate the stability of Zn foils across different solutions, Zn foils were immersed into the above two solutions for a duration of 10 days (240 h) and subsequently subjected to characterization. X-ray diffraction (XRD) results display a distinct and sharp peak at ≈8° belonging to the $Zn_4SO_4(OH)_6\bullet 5H_2O$ byproduct in the $ZnSO_4$ electrolyte, while only a tiny byproduct peak is seen in the $ZnSO_4$/NaDFOB electrolyte (**Figure 1a**). This observation is reinforced by scanning electron microscope (SEM) images, revealing a clean and smooth surface on the Zn foil soaked in the $ZnSO_4$/NaDFOB electrolyte, similar to the pristine Zn foil without soaking in the electrolyte (Figure 1b; Figure S6, Supporting Information). In contrast, a substantial number of hexagonal plates manifest on the Zn foil submerged in the $ZnSO_4$ electrolyte, aligning with the $Zn_4SO_4(OH)_6\bullet 5H_2O$ byproduct as confirmed by the energy-dispersive X-ray spectroscopy (EDX) spectrum (Figure S7, Supporting Information). Evidently, the introduction of NaDFOB exerts an effective suppression against corrosion and side reactions occurring on the Zn electrode surface. The restrained corrosion was further confirmed by the lower corrosion current (2.8 mA) and higher corrosion potential (0.03 V) observed in the Tafel plots of a Zn/Zn symmetric cell within the $ZnSO_4$/NaDFOB electrolyte as compared to the pure $ZnSO_4$ electrolyte (9.5 mA and 0.01 V, respectively) (Figure S8, Supporting Information). The ATR-FTIR results of the soaked Zn foil in $ZnSO_4$/NaDFOB electrolyte reveal the existence of C = O and C–O originating from $DFOB^-$ emerged

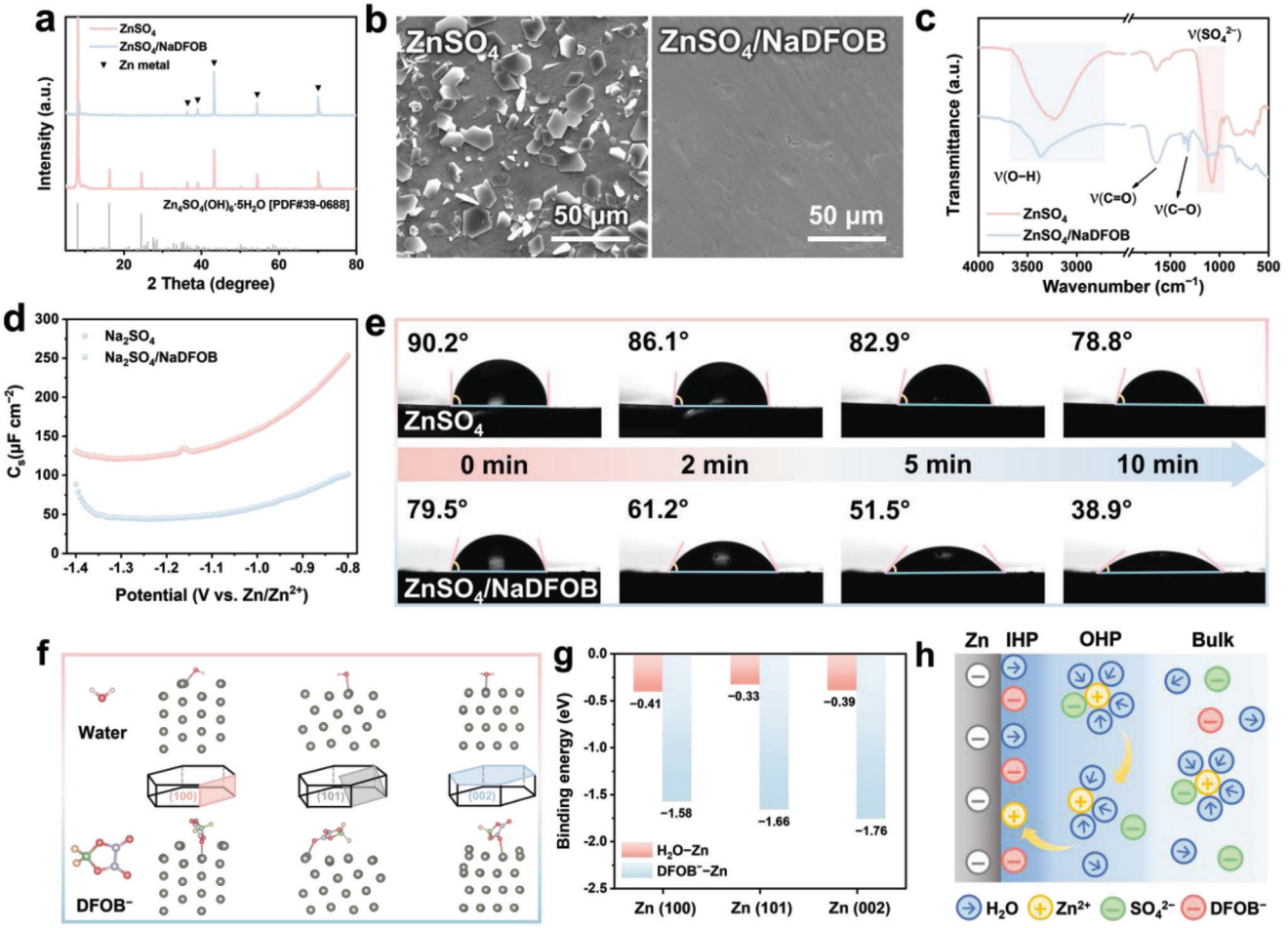

Figure 1. a) XRD patterns, b) SEM images, and c) ATR-FTIR spectra of the Zn foils after soaking in $ZnSO_4$ and $ZnSO_4$/NaDFOB electrolytes for ten days. d) Differential capacitance curves of Zn in Na_2SO_4 and Na_2SO_4/NaDFOB solutions. e) Contact angle measurements of $ZnSO_4$ and $ZnSO_4$/NaDFOB electrolytes at different measuring times. f) Adsorption states of $DFOB^-$ ions and H_2O molecules on the different Zn facets and g) corresponding adsorption energies. h) Schematic illustration of the interfacial structure in the $ZnSO_4$/NaDFOB electrolyte.

at 1639.2 and 1317.2 cm^{-1} in the $ZnSO_4$/NaDFOB electrolyte, respectively, demonstrating the presence of NaDFOB molecules adsorbed on the Zn surface (Figure 1c).[58] In contrast, a broad peak at 2700–3700 cm^{-1} represents the O–H vibration from the $Zn_4SO_4(OH)_6{\bullet}5H_2O$ byproduct after soaking in the $ZnSO_4$ electrolyte. The X-ray photoelectron spectroscopy (XPS) spectra of C 1s and O 1s show the presence of C–O and C = O functionalities on the surface, thereby confirming the adsorption of NaDFOB on the soaked Zn foil (Figure S9, Supporting Information). This specific adsorption can be attributed to a modification of the EDL by NaDFOB within the electrolyte.

To validate the adsorption behavior of NaDFOB onto the Zn surface, the non-Faradaic EDL capacitance of both electrolytes was measured, in which Na_2SO_4 replaced $ZnSO_4$ to eliminate a disturbance from the measurement of Faradaic current.[36,59] As illustrated in Figure 1d, the existence of NaDFOB in the $ZnSO_4$ electrolyte led to a notable reduction in surface capacitance. This reduction indicates that the EDL on the Zn surface became thicker because of the adsorption of NaDFOB molecules on the Zn surface.[30] Furthermore, the open circuit potentials of Zn foil when immersing it in the electrolytes were measured to assess the potential change on the Zn surface (Figure S10, Supporting Information). In the $ZnSO_4$ electrolyte, the open circuit potential exhibits a continuous rise, which is likely due to the migration of Zn^{2+} ions toward the Zn foil, which is negatively charged when immersed in the electrolyte.[60] In contrast, in the $ZnSO_4$/NaDFOB electrolyte, the open circuit potential experienced an initial short-time increase followed by a continuous decline until stabilizing after 350 s. The potential reduction can be attributed to the adsorption of $DFOB^-$ on the surface, which enables a more negative potential. Furthermore, as shown in the dynamic contact angle measurements (Figure 1e), the wettability of the $ZnSO_4$ electrolyte changed from 90.2° to 78.8° (12.6% change) over a span of 10 min. For comparison, the contact angles in the $ZnSO_4$/NaDFOB electrolyte experienced a drastic drop from 79.5° to 38.9° (51.1% change) within the same time, indicating a decreased interfacial free energy. The improved wettability is due to the moderate adsorption of $DFOB^-$ on the Zn surface, which serves as a surfactant adjusting the interface between Zn foil and the electrolyte.[61,62] The above findings indicate that the addition of NaDFOB modifies the Zn foil surface, achieved by a reconfiguration of the EDL structure.

DFT calculations provide additional evidence of $DFOB^-$ adsorbing on the Zn surface. The adsorption energies of both H_2O and $DFOB^-$ on different Zn facets unveil their interactions with the Zn electrode (Figure 1f). According to the results in Figure 1g, $DFOB^-$ ions have significantly larger binding energies with Zn than H_2O on any Zn facets presented experimentally, indicating that $DFOB^-$ adsorbs on the Zn surface more preferentially. The differential charge density distribution images further demonstrate the electronic interactions between O in $DFOB^-$ and the Zn metal (Figure S11, Supporting Information). Accordingly, $DFOB^-$ ions preferentially and stably attach to the Zn surface as compared to H_2O, thereby affecting the EDL with less water content.

MD simulation was conducted to visualize the structure of the EDL intuitively. As depicted in Figure S12a (Supporting Information), the simulation shows that six $DFOB^-$ ions are attached to the electrode surface, and the other three are in the bulk electrolyte. The tendency of adsorbing on the electrode surface of the $DFOB^-$ ions can be attributed to the high adsorption energy between the $DFOB^-$ and Zn electrodes. Additionally, the top view of the Helmholtz layer confirms the presence of $DFOB^-$ ions in the EDL (Figure S12b, Supporting Information). Overall, the MD simulation results provide strong evidence for the occupation of $DFOB^-$ ions in the EDL structure.

Based on the above results, the interfacial structures between the Zn electrode and electrolyte are illustrated in Figure 1h and Figure S13 (Supporting Information). Without $DFOB^-$ ions, water dipoles occupy the IHP, resulting in a water-rich EDL and facilitating water decomposition-related parasitic reactions (Figure S13, Supporting Information). In contrast, after introducing NaDFOB, $DFOB^-$ ions tend to adsorb on the Zn metal surface through O–Zn interactions (Figure 1h). Due to the occupation of $DFOB^-$, water molecules are squeezed out of the IHP, eventually establishing a water-poor EDL. Consequently, the $DFOB^-$-modified EDL is expected to suppress the side reactions and promote the sustainability of the Zn electrode. Meanwhile, due to the existence of $DFOB^-$ ions in the EDL, which blocks the charge transfer on the electrode-electrolyte interface, the ionic conductivity and Zn^{2+} transference number in the $ZnSO_4$/NaDFOB electrolyte are slightly lower than those of the $ZnSO_4$ electrolyte (Figures S14 and S15, Supporting Information).

2.2. Highly Uniform and Reversible Zn Deposition

To evaluate the reversibility and stability of Zn plating/stripping behavior, the CE of Zn/Cu half cells was measured. As presented in **Figure 2a**, the CE of the Zn/Cu battery in the $ZnSO_4$ electrolyte fluctuates for 200 cycles with an average value of 97.1%. The low CE is due to the emergence of parasitic reactions (i.e., HER, OER, and byproducts) that occurred on the electrode surface. In contrast, the Zn/Cu cell in the $ZnSO_4$/NaDFOB electrolyte demonstrated consistent performance, maintaining an average CE of 99.3% throughout 400 cycles (Figure S16, Supporting Information), indicating highly reversible Zn plating/stripping processes and effective suppression of side reactions. The evidence in the voltage profiles demonstrates a 14 mV reduction in potential polarization in the $ZnSO_4$/NaDFOB electrolyte in comparison to the pure $ZnSO_4$ electrolyte, illustrating enhanced plating/stripping kinetics in the $ZnSO_4$/NaDFOB electrolyte (Figure 2b).[63] This reduction in potential hysteresis within the $ZnSO_4$/NaDFOB electrolyte can be ascribed to the efficient mitigation of byproduct accumulation and the consequent alleviation of interfacial resistance due to the existence of the $DFOB^-$ ions, which occupy the water-poor EDL as DFT results have indicated, ultimately resulting in the elimination of side reactions associated with water decomposition.[64]

Optical Zn/Cu half cells were employed to visualize the Zn deposition behavior that transpired on the Cu foils under a current density of 2 mA cm^{-2} in different electrolytes (Figure 2c). In the $ZnSO_4$ electrolyte, a bubble became evident after 2 min of deposition and progressively expanded over the subsequent 8 min. Nonuniform shining spots attributed to the aggregation of Zn on the existing Zn-deposited sites appeared after 6 min, eventually forming Zn dendrites. However, in the $ZnSO_4$/NaDFOB electrolyte, neither bubbles nor Zn dendrites were present. Instead, only a change in the shininess and roughness of Cu foil was observable over 10 min. This surface modification on the Cu foil can be attributed to a super uniform Zn deposition devoid of dendrite growth. The Zn-deposited Cu foils are depicted in Figure 2d, illustrating the deposition distribution. In the $ZnSO_4$ electrolyte, the aggregation of Zn dendrites occurred at both the center and edges of the Cu foil, while the introduction of NaDFOB fostered an extremely uniform Zn deposition. The metallustrous and smooth surface denotes a homogenous distribution of Zn metal instead of Zn aggregation. 3D morphology profiles of the deposited foils show the dendrites reaching a height of 118.3 μm in $ZnSO_4$, whereas a flat surface is evident in the $ZnSO_4$/NaDFOB electrolyte (23.0 μm). The SEM images of the deposited Cu foils corroborate the above results, emphasizing the pivotal role of NaDFOB in achieving homogeneous Zn deposition. As seen in Figure 2e, a Zn dendrite with a diameter of ≈150 μm is observed in the $ZnSO_4$ electrolyte, which disengages from the Cu substrate. Moreover, the rough surface of Zn dendrite with nanosheet-like morphology reinforces the random Zn deposition (Figure S17, Supporting Information). In contrast, since the $DFOB^-$ anion-modified EDL is adaptable to the Zn deposition, a thin Zn layer with uniform surface is tightly attached to the Cu foil without any interspace (Figure 2e; Figure S17, Supporting Information). Cross-sectional SEM and EDX results, coupled with XRD patterns, present further insights indicating that the accumulation of byproducts only occurs in the $ZnSO_4$ electrolyte (Figures S18 and S19, Supporting Information). To assess the influence of Na^+ on Zn deposition, a Zn/Cu half cell employing the $ZnSO_4$/Na_2SO_4 electrolyte was examined, which exhibits nonuniform Zn dendrites at the Cu edge, representing the limited impact of Na^+ on Zn deposition (Figure S20, Supporting Information). Therefore, under the regulation of adsorbed $DFOB^-$ anions, the Zn deposition manifests enhanced uniformity.

2.3. Progressive Nucleation in the $ZnSO_4$/NaDFOB Electrolyte

A series of electrochemical measurements, including cyclic voltammetry (CV), nucleation overpotential testing, and chronoamperometry (CA), were undertaken to evaluate the nucleation characteristics and underlying mechanism behind the

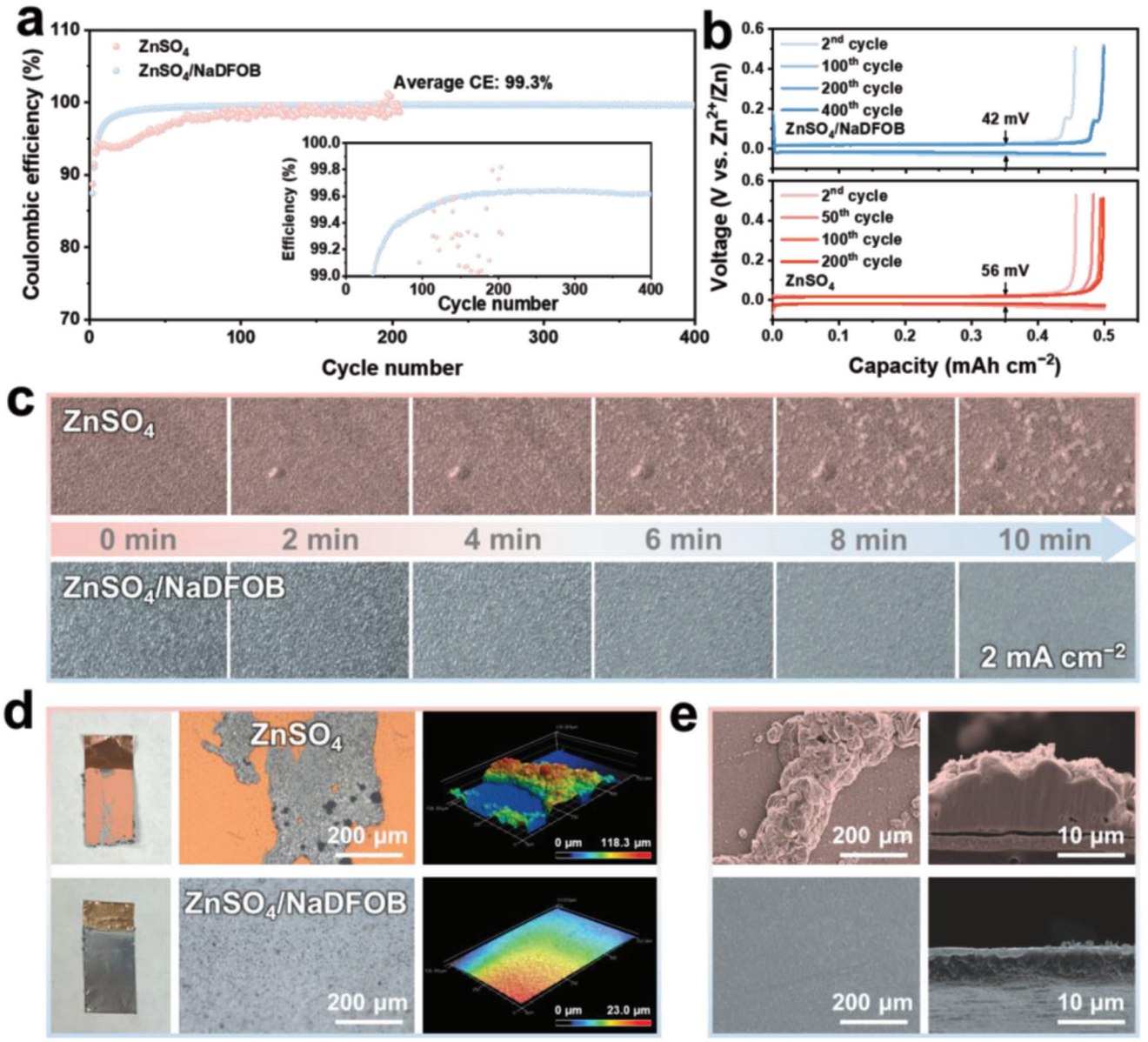

Figure 2. a) CE of Zn/Cu half cells cycled at a current density of 1 mA cm^{-2} to achieve an areal capacity of 0.5 mAh cm^{-2} in the $ZnSO_4$ electrolyte with/without NaDFOB additive, and b) corresponding voltage profiles at different cycles in both electrolytes. c) In situ optical images of the Zn deposited Cu foils in Zn/Cu half cells in both electrolytes at a current density of 2 mA cm^{-2}. d) Optical images and 3D topographic images of Zn-deposited Cu foils with a depositing capacity of 5 mAh cm^{-2} at a current density of 1 mA cm^{-2}, and e) corresponding SEM images of Zn-deposited Cu foils.

deposition within both electrolytes. The initial-cycle CV curves of Zn/Ti half cells are illustrated in **Figure 3**a. In both electrolytes, a pair of redox peaks with similar area and slope can be observed at almost the same position, indicating that the addition of NaDFOB barely changes the kinetics of Zn plating/stripping. However, the existence of NaDFOB plays an important role in the stability and reversibility of Zn plating/stripping. As shown in Figure S21a (Supporting Information), with the presence of NaDFOB in the electrolyte, the overlap of the CV curves at different cycles indicates that the Zn/Ti half-cell within the $ZnSO_4$/NaDFOB electrolyte exhibits remarkable reversibility during Zn plating/stripping. In contrast, the signal of side reactions starts to be observed at the 5th cycle in the $ZnSO_4$ electrolyte, followed by the feature of water decomposition in the next cycles (Figure S21b, Supporting Information).[65] Rather than the different stability, the electrolyte containing NaDFOB possesses a more negative onset potential of −0.24 V than the pure $ZnSO_4$ electrolyte (−0.11 V) in the first cycle, representing a higher driving force for nucleation and lower activity for the HER.[66] Similarly, the potential-time curves under galvanostatic Zn electrodeposition show a higher nucleation overpotential and a more homogeneous Zn deposition with the $ZnSO_4$/NaDFOB electrolyte (Figure 3b). It has been reported that the initial nucleation overpotential can determine the subsequent Zn growth and

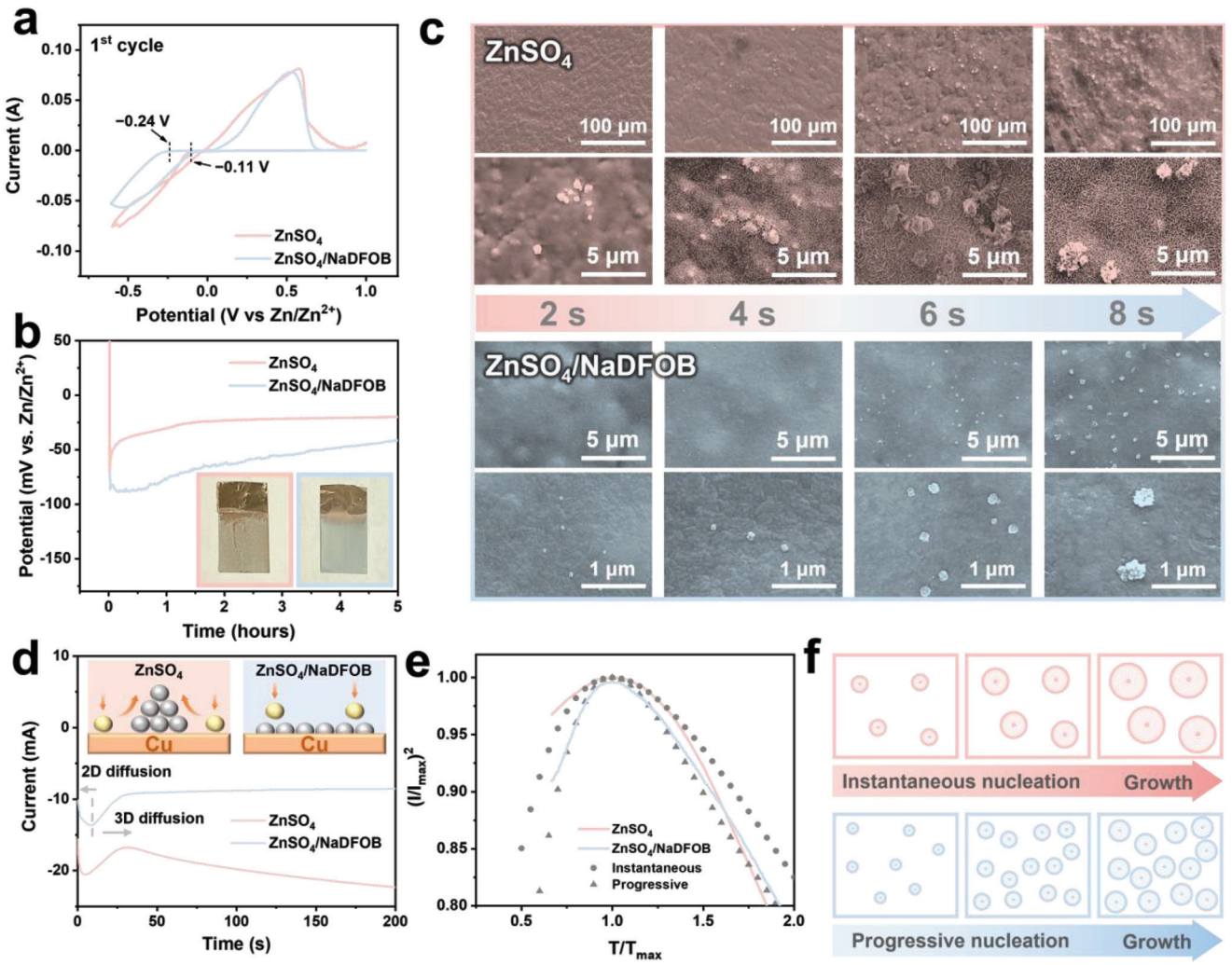

Figure 3. a) CV curves of the first cycle in Zn/Ti half cells in $ZnSO_4$ and $ZnSO_4$/NaDFOB electrolytes at a scan rate of 0.1 mV s^{-1}. b) Voltage profiles of galvanostatic Zn deposition on the Cu foils at 1 mA cm^{-2} to reach 5 mAh cm^{-2}. The insets are optical images of the Zn-deposited Cu foils. c) Ex situ SEM images of Zn nucleation and growth process at different times on the Cu foil in the $ZnSO_4$ electrolytes with/without NaDFOB additive. d) CA curves at −200 mV in Zn/Cu half cells in both electrolytes. Insets are schematic illustrations of Zn^{2+} diffusion modes in different electrolytes. e) Theoretical dimensionless plots for instantaneous and progressive nucleation and experimental dimensionless curves derived from CA curves in $ZnSO_4$ and $ZnSO_4$/NaDFOB electrolytes. f) Schematic illustration of Zn nucleation and growth with instantaneous and progressive nucleation.

eventual morphology.[52,53] Hence, it is necessary to delve into the influence of $DFOB^-$ ions on Zn nucleation in accordance with nucleation-growth theory. Intrinsically, the relationship between nucleation overpotential (η_n) and the radius of the Zn nuclei (r) has been summarized as follows:[52,56,67]

$$r = \frac{3V_m\gamma_{sl}}{F|\eta_n|} \quad (1)$$

where r is the radius of the Zn nuclei, V_m represents the molar volume of Zn, γ_{sl} represents the surface energy of the Zn foil, and F is Faraday's constant. According to Young's equation and Fowkes equation, the surface energy γ_{sl} can be calculated with the following equation:[68,69]

$$\gamma_{sl} = \gamma_{sg}\left(\frac{1-\cos\theta}{1+\cos\theta}\right)^2 \quad (2)$$

where θ is the contact angle and γ_{sg} is the surface tension of the Zn foil. Accordingly, the derived equation is summarized as:

$$r = \frac{3V_m\gamma_{sg}}{F|\eta_n|}\, tan^4\left(\frac{\theta}{2}\right) \quad (3)$$

Evidently, the dimensions of the Zn nuclei are intrinsically linked to both the nucleation overpotential and the wettability between the electrolyte and the electrode. In particular, an increase in overpotential coupled with a decrease in contact angle corresponds to the formation of smaller Zn nuclei (Figure S22, Supporting Information). According to the contact angle results in Figure 1e and the overpotential profiles in Figure 3b, the interrelation between the nuclei radius and nucleation overpotential is presented in Figure S23 (Supporting Information).

This graphical representation demonstrates a trend wherein the radius of the Zn nuclei in the $ZnSO_4$/NaDFOB electrolyte consistently remains smaller than that in pure $ZnSO_4$ electrolyte.

The nucleation process and subsequent growth of Zn nuclei were investigated through ex situ SEM. Figure 3c shows the Zn deposition behavior on the Cu foils under a constant current condition within a time range of 2 to 8 s. In the $ZnSO_4$ electrolyte, an increase in the size of the Zn nuclei was observed as the deposition time increased, especially in the zoomed-in images depicted with the 5 µm scale bar. The early-stage nuclei show a spherical morphology with an average diameter of 0.5 µm, which transformed into larger grains with an irregular nanoflower-like shape after 6 s. Additionally, uniformly covered nanosheets can be observed after 4 s. The EDX results of the Cu foil after depositing 6 s demonstrate that the nanoflower-like structure corresponds to the Zn nuclei, and the nanosheets represent sulfate-hydroxide-based byproducts (Figure S24, Supporting Information). In contrast, the presence of Zn nuclei in the $ZnSO_4$/NaDFOB electrolyte can only be found in the 5 µm scale bar images, indicating a reduction in nuclei size due to the addition of NaDFOB. The distribution of Zn nanospheres is notably more uniform compared to that in the $ZnSO_4$ electrolyte, attributed to the regulatory effect of adsorbed $DFOB^-$ ions. Detailed observations of morphology in the 1 µm scale bar images highlight a progressive growth of Zn nuclei from 65 to 335 nm. Additionally, the Cu foil surfaces remain clean without any formation of nanosheet-like byproducts, indicating effective suppression of parasitic reactions by the adsorbed $DFOB^-$. Notably, comparative and quantitative analysis of the average nuclei sizes reveals that, in contrast to the $ZnSO_4$ electrolyte, Zn grain sizes at varying deposition times were significantly smaller and more evenly distributed when NaDFOB was introduced (Figure S25, Supporting Information). This result confirms that $DFOB^-$ modification can be crucial for controlling the nucleation and growth of Zn nanoparticles. The refined Zn grain growth, along with the uniform distribution of deposition sites, facilitates homogeneous deposition, resulting in a smooth surface with a distinct metallic luster on the Zn-deposited Cu foil, as demonstrated in Figure 2d.

To understand the mechanism governing Zn nucleation behavior in different electrolytes, CA measurements were conducted. Figure 3d exhibits the time-dependent current change with the application of a constant voltage of −200 mV. At the beginning stage, both curves demonstrate a current increase followed by peak currents, indicating the characteristic 2D nucleation and growth of Zn nuclei.[70,71] Upon surpassing the peak current in the $ZnSO_4$/NaDFOB electrolyte, a continuous current decrease followed by a steady state can be observed, corresponding to the diffusion limitation-controlled nucleation process.[72–77] The decreased current can be ascribed to the 3D Zn diffusion induced by the adsorbed $DFOB^-$.[73,78,79] Specifically, the adsorption of $DFOB^-$ provided an additional hindrance restricting the diffusion of Zn^{2+}, which was confirmed by the slightly lower ionic conductivity and smaller Zn^{2+} transference number of the $ZnSO_4$/NaDFOB electrolyte in comparison to the $ZnSO_4$ electrolyte (Figures S14 and S15, Supporting Information). Consequently, Zn^{2+} ions tended to nucleate at the adsorption sites rather than diffusing toward pre-existing nuclei and accumulating as Zn dendrites. This process requires a low energy and consequently induces a decrease of current. In contrast, within the $ZnSO_4$ electrolyte, an initial drop in current was followed by a sustained rise. Absent the influence of $DFOB^-$ adsorption, the Zn^{2+} ions are inclined to diffuse along the surface, actively seeking favorable sites for nucleation, primarily the pre-existing Zn nuclei.[80,81] Accordingly, the current continuously increases to offer a driving force to overcome the extra energy barrier for diffusion. The accumulation of Zn on the limited pre-existing Zn nuclei finally leads to Zn dendrites.

Scharifker introduced the theory of 3D nucleation coupled with subsequent diffusion-controlled growth, which encompasses two nucleation models: instantaneous nucleation and progressive nucleation.[73,74,82,83] Specifically, instantaneous nucleation represents the process in which all the nuclei emerge simultaneously at adsorption sites and then grow at the same rate. Conversely, progressive nucleation characterizes a process where the nucleation sites activate progressively. As the existing nuclei grow, new nuclei continue to form, resulting in a continuous generation of the nucleation process. According to the Scharifker-Hills (S-H) model for potentiostatic transients, the instantaneous and progressive nucleation can be expressed as following dimensionless equations:[82,84]

Instantaneous nucleation:

$$\left(I/I_m\right)^2 = 1.9542(t/t_m)^{-1}\left\{1 - exp\left[-1.2564\left(t/t_m\right)\right]\right\}^2 \quad (4)$$

Progressive nucleation:

$$\left(I/I_m\right)^2 = 1.2254(t/t_m)^{-1}\left\{1 - exp\left[-2.3367(t/t_m)^2\right]\right\}^2 \quad (5)$$

where I and t are current and time, respectively, and I_m and t_m are the maximum current and corresponding time. By comparing the normalized dimensionless form $(I/I_m)^2$ versus (t/t_m) curves derived from CA measurement and theoretical equations, the nucleation modes in different electrolytes can be determined. As depicted in Figure 3e, before $t/t_m = 1$, the curve of $ZnSO_4$/NaDFOB fits with the progressive nucleation model perfectly, while the curve of normal $ZnSO_4$ electrolyte is close to the model of instantaneous nucleation. These distinctive results substantiate the occurrence of disparate nucleation modes upon the introduction of NaDFOB into the electrolyte. Moreover, in the region after $t/t_m = 1$, the curve for $ZnSO_4$/NaDFOB remains consistent with the theoretical result, whereas the curve without NaDFOB deviates from the theoretical model due to the uneven electrode surface.[60] These nucleation modes correlate with previously observed nucleation overpotential profiles. The nucleation overpotential curve of $ZnSO_4$ in Figure 3b shows a pronounced peak at the initial stage, representing a fast nucleation process. Subsequent potential reduction signifies the crystal growth at the pre-existing nuclei sites. In contrast, the voltage profile for $ZnSO_4$/NaDFOB manifests a plateau featuring a similar peak overpotential for the initial 30 min. This prolonged elevation of overpotential continually provides a driving force to cross over the energy barrier required for the nucleation. The maintenance of the high overpotential demonstrates the progressive nucleation that occurred with the regulation of $DFOB^-$. Summarily depicted in Figure 3f, in the $ZnSO_4$ electrolyte, a finite number of nucleation sites existed, rapidly occupied by the Zn nuclei in a very short span. The nucleation process stopped once all the sites were utilized, with Zn preferentially deposited on the existing nuclei to

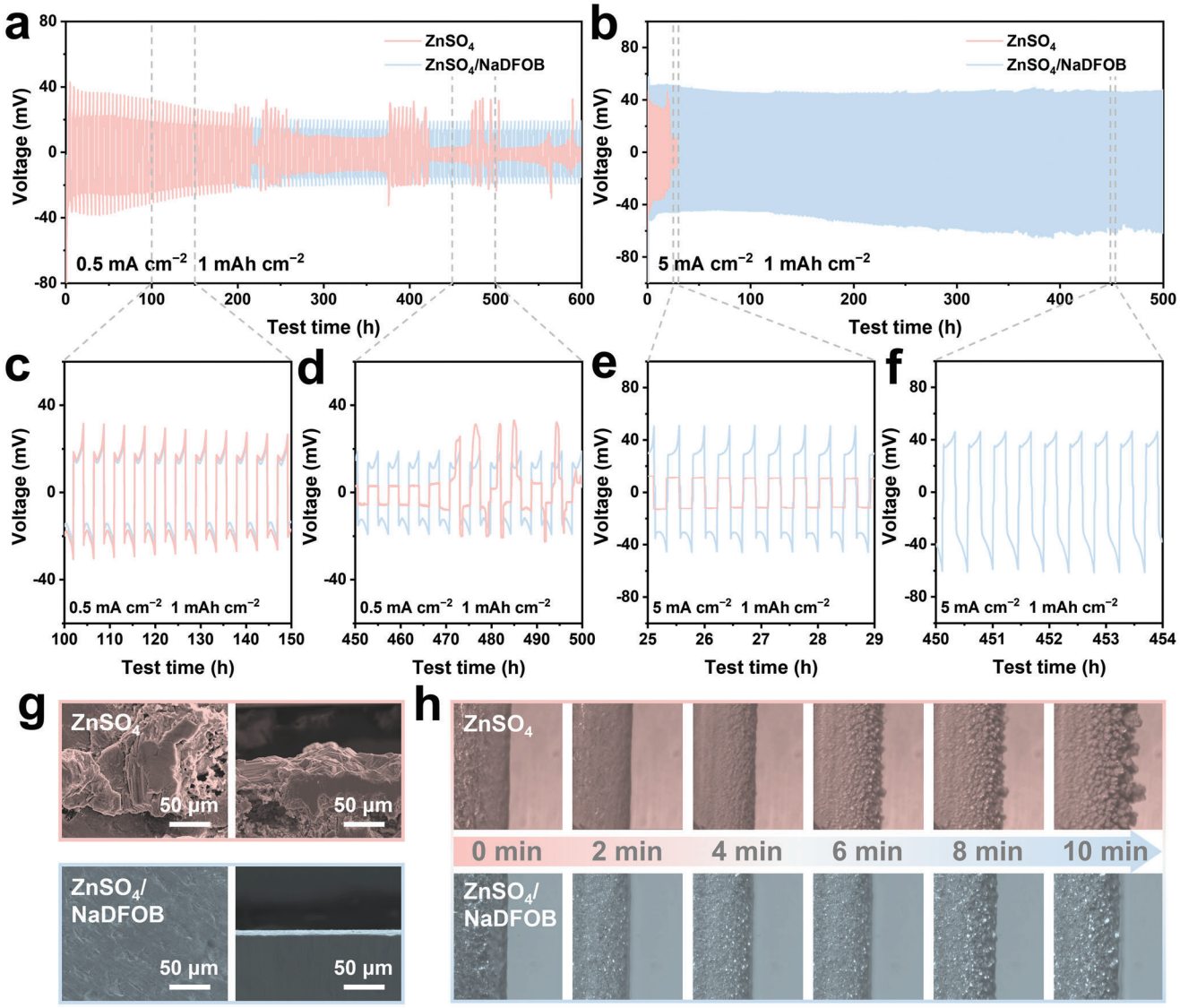

Figure 4. Cycling performance of Zn/Zn symmetric cells and corresponding selected voltage profiles at certain cycles at a,c, and d) 0.5 mA cm^{-2} and (b,e, and f) 5 mA cm^{-2} to achieve a capacity of 1 mAh cm^{-2}. g) Normal and cross-sectional SEM images of Zn electrodes cycled in different electrolytes at 0.5 mA cm^{-2}. h) In situ images of Zn/Zn optical cells in different electrolytes at different times.

foster Zn dendrite growth. In contrast, the adsorption of $DFOB^-$ on the electrode surface introduced more nucleation sites, due to which the nucleation occurred continuously throughout the Zn deposition process, resulting in smaller grain sizes. Consequently, the distribution of Zn nuclei is more evenly dispersed, and the following Zn growth is uniform without Zn dendrites or aggregation.

2.4. Electrochemical Performance in Zn/Zn Symmetric Cells

Zn/Zn symmetric cells were assembled and tested to evaluate the influence of the nucleation mode on the Zn electrode. Incorporating NaDFOB into the $ZnSO_4$ electrolyte led to a notable improvement in the cycling stability of Zn/Zn symmetric cells. As shown in **Figure** 4a, the battery within the $ZnSO_4$/NaDFOB electrolyte exhibits extended cycling durability over 600 h at a current density of 0.5 mA cm^{-2} to achieve a capacity of 1 mAh cm^{-2}. In contrast, Zn/Zn symmetric cells in the pure $ZnSO_4$ electrolyte managed only 200 h of cycling with a notable failure. An examination of the voltage profiles after 100 h unveils a higher overpotential present in the $ZnSO_4$ electrolyte, which can be ascribed to a nonuniform Zn surface with pits and dendrites (Figure 4c). Moreover, the occurrence of a short circuit and a sharp increase in overpotential after 450 h is evident, indicating the penetration of Zn dendrites through the membrane and the formation of dead zinc (Figure 4d).[85] Similarly, even at an elevated current density of 5 mA cm^{-2}, the battery in the electrolyte with NaDFOB additive sustained a consistent cycling performance for over 500 h. In contrast, the battery in pure $ZnSO_4$ only cycled for 20 h with a subsequent short circuit (Figure 4b,e, and f). Furthermore, the battery cycled within the $ZnSO_4$/NaDFOB electrolyte exhibited a stable

cycling for over 500 h at 5 mA cm^{-2} to reach a higher areal capacity of 10 mAh cm^{-2} (Figure S26, Supporting Information). This indicates that the addition of NaDFOB can effectively enhance the reversibility and stability of Zn plating and stripping. Notably, the polarization profiles shown in Figure 4a and Figure S26 (Supporting Information) display higher overpotential when using the $ZnSO_4$ electrolyte, while the $ZnSO_4$/NaDFOB electrolyte has greater overpotential than the $ZnSO_4$ electrolyte in Figure 4b. This discrepancy in the overpotential can be attributed to the varying plating/stripping time.[86] A longer depositing time results in a greater accumulation of pits and dendrites on the electrode surface in the $ZnSO_4$ electrolyte, showing higher overpotentials in Figure 4a and Figure S26 (Supporting Information).

For a visual assessment of alterations on the Zn electrode surface, SEM analysis was conducted. An obvious Zn dendrite with a diameter over 200 µm was found on the Zn anode surface cycled in the $ZnSO_4$ electrolyte (Figure 4g). In contrast, the deposited Zn modified the pristine Zn with a more uniform, flattened, and homogeneously textured surface within the $ZnSO_4$/NaDFOB electrolyte (Figure S27, Supporting Information). The super-uniform Zn deposition in the cross-sectional SEM image confirms the even Zn plating and stripping with the addition of NaDFOB in the electrolyte. However, a cross-sectional image of the Zn anode in the $ZnSO_4$ electrolyte shows the emergence of dendritic structures and voids across the Zn foil surface. Distinctive Zn deposition behaviors in both electrolytes were monitored by in situ optical Zn/Zn symmetric cells by applying a constant current density of 5 mA cm^{-2} (Figure 4h). Upon 6 min of Zn plating, Zn dendrites are found on the Zn surface with subsequent growth in the following 4 min. In comparison, the Zn surface immersed in the $ZnSO_4$/NaDFOB electrolyte remained flat and uniform for a duration of 10 min, confirming the impact of NaDFOB in facilitating advantageous Zn deposition.

2.5. Zn Deposition Kinetics and Formation of SEI Layer

In addition to showcasing the cycling performance at constant current densities of 0.5 and 5 mA cm^{-2}, **Figure 5a** displays the rate performances at various current densities from 0.5 to 5 mA cm^{-2} in different electrolytes. The battery with the $ZnSO_4$/NaDFOB electrolyte cycled stably at different current densities without encountering any failure, while voltage polarization and a short circuit occurred at high current densities (i.e., 4 and 5 mA cm^{-2}) within the $ZnSO_4$ electrolyte, indicating inferior reversibility of Zn plating/stripping in the $ZnSO_4$ electrolyte. Notably, the battery in $ZnSO_4$/NaDFOB electrolyte consistently displayed a lower overpotential than pure $ZnSO_4$ electrolyte at each current density. The smaller voltage hysteresis indicates accelerated reaction kinetics of Zn deposition, coupled with sustained uniformity of Zn electrodes. To quantitatively assess the kinetics alteration following the addition of NaDFOB into the electrolyte, the exchange current density related to Zn deposition, which illustrates the rate of redox reactions taking place on the electrode surface under equilibrium potential, was calculated based on the following equation:[87,88]

$$i = i_0 \frac{F}{2RT}\eta \quad (6)$$

where i is the experimental current density, i_0 is the exchange current density, F is the Faraday constant, R is the gas constant, T is the temperature (K), and η is the measured overpotential. The exchange current density values derived from calculations in Figure 5b reveal a notable contrast between the $ZnSO_4$/NaDFOB electrolyte (29.7 mA cm^{-2}) and pure $ZnSO_4$ (16.5 mA cm^{-2}), which demonstrates the rapid kinetics of Zn deposition within the $ZnSO_4$/NaDFOB electrolyte. The enhanced Zn transport and Zn deposition kinetics in $ZnSO_4$/NaDFOB are confirmed by electrochemical impedance spectroscopy (EIS) measurements conducted on Zn/Zn symmetric cells at different temperatures (Figure 5c; Figure S28, Supporting Information). Comparative analysis shows that the impedance values in the $ZnSO_4$/NaDFOB electrolyte are lower than in the $ZnSO_4$ electrolyte across all temperatures, indicating a reduced electron transfer barrier and improved ionic transport at the electrode surface in the $ZnSO_4$/NaDFOB electrolyte (Figure S29, Supporting Information). Based on the EIS results and the Arrhenius equation, the activation energy (E_a) for charge transfer on the electrode surface was determined by fitting the linear relationship between resistance and temperature (Figure 5d). The activation energy for the Zn electrode in the $ZnSO_4$/NaDFOB electrolyte (41.6 kJ mol^{-1}) is lower than that within the $ZnSO_4$ electrolyte (47.9 kJ mol^{-1}), reinforcing the notion that the addition of NaDFOB is beneficial to the kinetics on the electrolyte-electrode interface, even though the $ZnSO_4$/NaDFOB electrolyte exhibits lower ionic conductivity and Zn^{2+} transference number than the $ZnSO_4$ electrolyte.

Several factors, including temperature, surface characteristics, adsorbed species, and gas evolution, can influence interfacial reaction kinetics.[89,90] Considering the parasitic reactions induced by water decomposition, it is assumed that the slow reaction kinetics and Zn^{2+} transport in the $ZnSO_4$ electrolyte are due to the HER and byproducts that occurred on the electrode surface, which blocked mass transfer between electrolyte and electrode. Linear sweep voltammetry (LSV) assessments carried out in Zn/stainless steel half cells showcase a more negative onset overpotential for the $ZnSO_4$/NaDFOB electrolyte than the $ZnSO_4$ electrolyte at 10 mA, indicating easier generation of hydrogen gas within the pure $ZnSO_4$ electrolyte (Figure S30, Supporting Information). Similarly, as previously exhibited in the Tafel plots, the lower corrosion current (2.8 mA) of Zn/Zn symmetric cells within the $ZnSO_4$/NaDFOB electrolyte indicates effective suppression of hydrogenation corrosion (Figure S8, Supporting Information).[91] More intuitively, the Zn/Zn symmetric cell with the $ZnSO_4$ electrolyte expanded after cycling at 0.5 mA cm^{-2}, which is attributed to the formation of hydrogen gas (Figure S31, Supporting Information). As a comparison, the thickness of the battery barely changed when using the $ZnSO_4$/NaDFOB electrolyte due to the suppressed HER. The small hydrogen bubbles may adsorb onto the Zn electrode surface, thereby impeding the charge transfer between electrode and electrolyte and eventually decelerating the interfacial reaction kinetics.[92–94]

In addition to the influence of generated gas, the accumulation of the byproducts resulting from electrolyte decomposition may also modify the electrolyte-electrode interface to affect Zn^{2+} transport. Different techniques were carried out to characterize and evaluate the electrode-electrolyte interface. The XRD pattern of the Zn electrode cycled in $ZnSO_4$ reveals

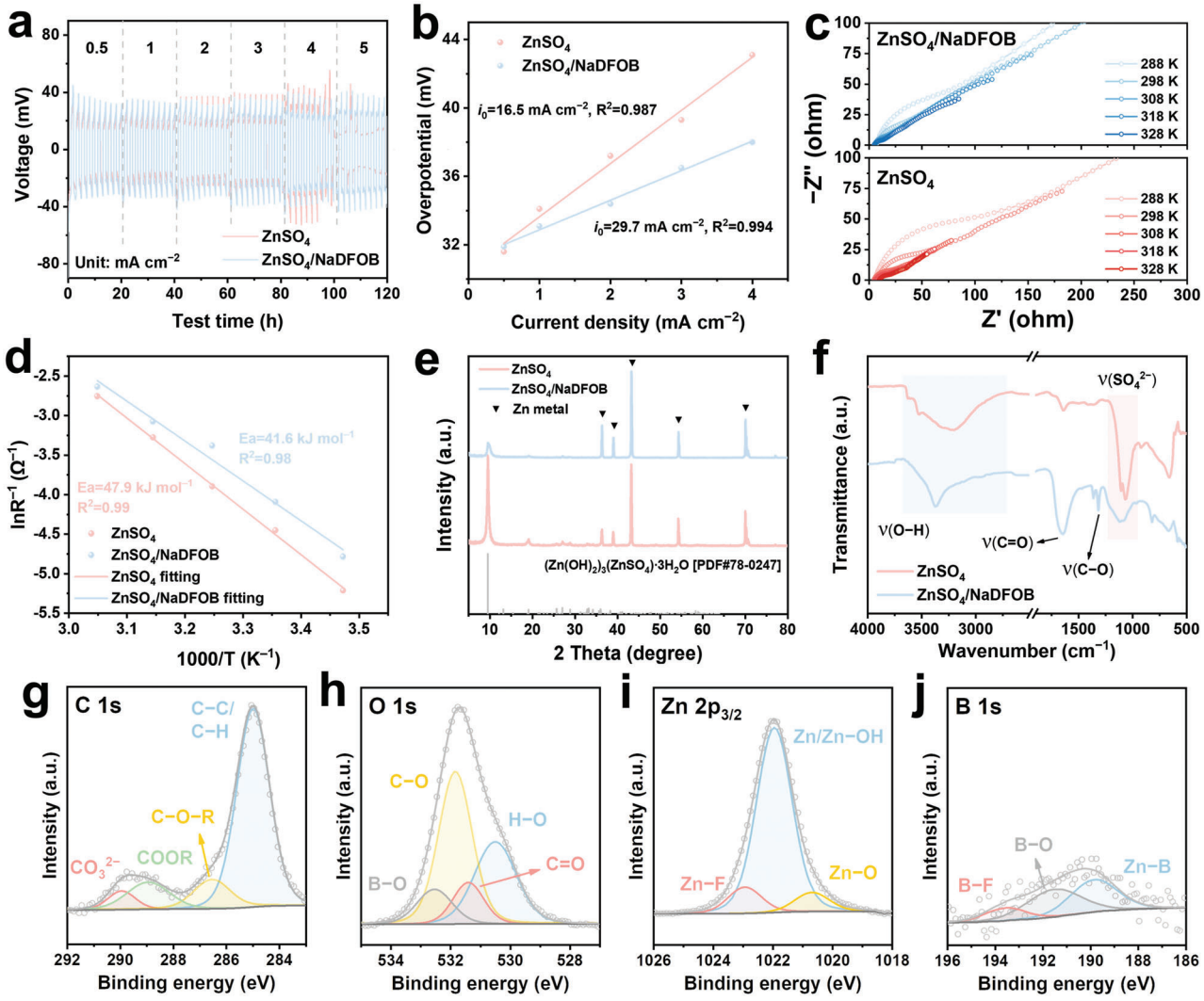

Figure 5. a) Cycling performance of Zn/Zn symmetric cell with various current densities in $ZnSO_4$ and $ZnSO_4$/NaDFOB electrolytes. b) Corresponding plots of overpotential versus current density of both electrolytes. c) Nyquist plots at different temperatures of Zn/Zn symmetric cells under different temperatures and d) corresponding fitting curves of $ZnSO_4$ and $ZnSO_4$/NaDFOB electrolytes based on the Arrhenius equation. e)XRD patterns, f) FTIR spectra, and XPS spectra of g) C 1s, h) O 1s, i) Zn $2p_{3/2}$, and j) B 1s for Zn electrodes from Zn/Zn symmetric cells cycled in the $ZnSO_4$/NaDFOB electrolyte.

a distinct peak centered ≈9°, which can be assigned to the $(Zn(OH)_2)_3(ZnSO_4)•3H_2O$ byproducts arising from water decomposition (Figure 5e). The deposition of these byproducts on the Zn surface blocked the charge transfer, leading to elevated activation energy and sluggish reaction kinetics. In contrast, a diffraction peak at the same degree with a tiny signal was observed in the $ZnSO_4$/NaDFOB electrolyte, indicating drastic suppression of parasitic reactions. The O–H and SO_4^{2-} vibrations from ATR-FTIR results of the cycled Zn surface verify the formation of $(Zn(OH)_2)_3(ZnSO_4)•3H_2O$ byproducts in the $ZnSO_4$ electrolyte (Figure 5f). Alongside the reduced intensities of two bands within the $ZnSO_4$/NaDFOB electrolyte, distinctive peaks associated with C = O and C–O vibrations appeared at 1645.0 and 1317.2 cm^{-1}, respectively, which may be attributed to the formation of a SEI layer.

To better understand the composition of this surface layer, XPS was employed to analyze the Zn electrode surface cycled in the $ZnSO_4$/NaDFOB electrolyte. To mitigate the influence of adsorbed $DFOB^-$ species, the Zn electrode was washed with deionized water three times to remove all the $DFOB^-$ species. The collected XPS spectra included C 1s, O 1s, Zn 2p, B 1s, and F 1s signals. In the C 1s spectrum, the C–C signal at 285 eV can be assigned to atmospheric carbon adsorbed on the sample surface when transferring the samples (Figure 5g).[95] The CO–R species and CO_3^{2-} component detected in both C 1s and O 1s spectra arise from the breakdown of $DFOB^-$ ions (Figure 5h). [96] The Zn 2p and F 1s spectra reveal the formation of Zn–F species corresponding to the inorganic ZnF_2 compound (Figure 5i; Figure S32, Supporting Information).[38] Furthermore, the Zn–OH and Zn–O components correlate to the coordination between Zn/OH^- and Zn/SO_4^{2-} within the tiny amount of $(Zn(OH)_2)_3(ZnSO_4)•3H_2O$ byproduct. The minor peaks within the B 1s spectrum align with other spectra in which $DFOB^-$ experienced electrochemical decomposition during

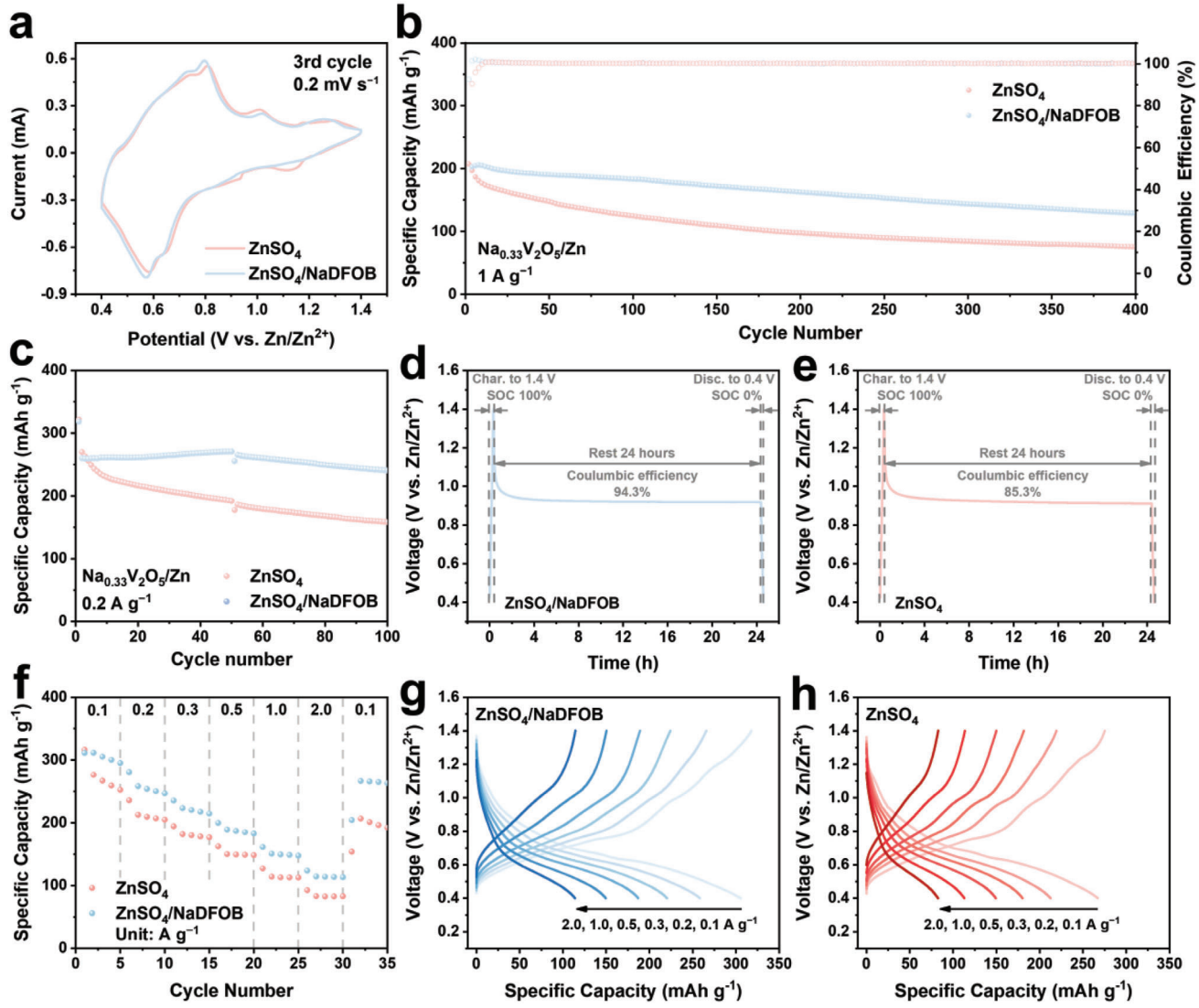

Figure 6. a) CV curves of the third cycle in NaVO/Zn full cells at a scan rate of 0.2 mV s^{-1} in $ZnSO_4$ and $ZnSO_4$/NaDFOB electrolytes. b) Cycling performance at a current density of 1 A g^{-1} and c) cycling performance at 0.2 A g^{-1} with resting for 24 h at the 50th cycle in different electrolytes. Corresponding voltage profiles of the 50th cycle in d) $ZnSO_4$/NaDFOB and e) $ZnSO_4$ electrolytes. f) Rate performance of NaVO/Zn full cells and corresponding voltage profiles of the batteries cycled in g) $ZnSO_4$/NaDFOB and h) $ZnSO_4$ electrolytes.

cycling (Figure 5j). The slight intensity of F 1s and B 1s signals may be attributed to the tiny concentration of $DFOB^-$ in the electrolyte (0.05 M). In contrast, when cycling the Zn foil in the $ZnSO_4$ electrolyte, only the atmospheric carbon species are visible in the C 1s spectrum (Figure S33a, Supporting Information). Moreover, the O 1s spectrum shows the presence of S = O, O−H, and Zn−O species, indicating the formation of sulfate hydroxide byproduct (Figure S33b, Supporting Information). This is also confirmed by the coordination of Zn−O and Zn−OH in the Zn 2p spectrum (Figure S33c, Supporting Information). Based on the above results, the formation of a $(Zn(OH)_2)_3(ZnSO_4)\cdot 3H_2O$ byproduct in the $ZnSO_4$ electrolyte is in contrast with the formation of an inorganic SEI layer due to the decomposition of $DFOB^-$ within the $ZnSO_4$/NaDFOB electrolyte, which passivated the Zn electrode to minimize the parasitic reactions. Additionally, this SEI layer facilitated the charge transfer, Zn^{2+} transport, and subsequent Zn deposition kinetics. Demonstrating this enhancement, Zn/Zn symmetric cells employing the $ZnSO_4$/NaDFOB electrolyte after cycling 10 and 20 cycles maintained a lower impedance, confirming the existence of the SEI layer can boost the charge transfer (Figure S34, Supporting Information). Further, the contact angles of cycled Zn electrodes illustrate that the wettability of the interface has been significantly promoted by the in-situ formed SEI layer, thereby promoting lower interfacial energy and facilitating Zn nucleation and deposition (Figure S35, Supporting Information).

2.6. Electrochemical Performance in $Na_{0.33}V_2O_5$/Zn Full Cells

The full cells employing $Na_{0.33}V_2O_5$ (NaVO) as a cathode were assembled to evaluate the practicality of the $ZnSO_4$/NaDFOB

electrolyte in zinc-ion batteries. NaVO cathode materials were synthesized as reported in the previous report.[97] The nanobelt-like morphology, as confirmed by SEM, and the presence of the pure $Na_{0.33}V_2O_5$ phase (PDF#48-0382), as detected through XRD, demonstrate the successful preparation of the NaVO cathode materials (Figure S36, Supporting Information). CV curves recorded at 0.2 mV s^{-1} for NaVO/Zn full cells exhibit redox peak pairs with nearly the same position and intensity on the cathode sides for both electrolytes, confirming that the cathodic redox reactions remain unaffected by the presence of NaDFOB (**Figure 6a**; Figure S37, Supporting Information). Moreover, the galvanic cycling performance of different electrolytes at 1 A g^{-1} exhibits similar initial capacity but different stability trends (Figure 6b). Specifically, the NaVO/Zn battery within the $ZnSO_4$/NaDFOB electrolyte maintained a capacity retention of 70%, while the $ZnSO_4$ electrolyte only retained 35% after 400 cycles. The more drastic capacity fading in the $ZnSO_4$ electrolyte is attributed to a more severe dissolution of the cathode material. To verify the limited dissolution in the NaDFOB-added electrolyte, cathodes were immersed in both electrolytes for one week. Notably, as indicated in Figure S38 (Supporting Information), the color of the $ZnSO_4$ electrolyte transitioned to a noticeable yellow after seven days, while the $ZnSO_4$/NaDFOB electrolyte maintained its transparency without any color change over the same period. This clear differentiation indicates that the NaDFOB additive exerts a positive impact on suppressing cathode dissolution in the aqueous electrolyte.[98,99] Further, the $ZnSO_4/Na_2SO_4$ electrolyte after soaking the NaVO cathode for seven days exhibits a relatively light-yellow color compared with the pure $ZnSO_4$ electrolyte, indicating that Na^+ can decrease the cathodic dissolution but cannot fully suppress it. Similar to the modulation of the EDL on the Zn anode surface, the presence of $DFOB^-$ brings about water-poor EDL remodification, leading to reduced water content near the cathode surface and effectively suppressing the cathodic dissolution.

The superior cycling stability of NaVO/Zn batteries in the $ZnSO_4$/NaDFOB electrolyte is further emphasized in Figure 6c, where the batteries were rested for 24 h after 50 cycles. After a 24 h rest, the capacity in the subsequent 50 cycles in the $ZnSO_4$/NaDFOB electrolyte still maintained a high retention of 93%, a considerable improvement over the $ZnSO_4$ electrolyte (58%). Further, the voltage profiles during the resting period reveal that the battery in the $ZnSO_4$/NaDFOB electrolyte displays an elevated CE (94%), demonstrating the suppressed parasitic reactions on the anode surface and the confined dissolution on the cathode side after adding NaDFOB in the electrolyte (Figure 6d and e). The rate performance further confirms the advantage of $ZnSO_4$/NaDFOB electrolyte under varying current densities, with consistently higher specific capacity achieved at each current in comparison to the $ZnSO_4$ electrolyte (Figure 6f). Notably, the capacity recovery rate at 0.1 A g^{-1} following cycling at 2 A g^{-1} in the $ZnSO_4$/NaDFOB electrolyte reaches 89%, higher than that in the $ZnSO_4$ electrolyte (73%), indicating enhanced reaction kinetics. The corresponding galvanic charge-discharge curves at different current densities imply a higher capacity and lower polarization in the $ZnSO_4$/NaDFOB electrolyte, which minimizes capacity loss (Figure 6g and h). In general, it is confirmed that adding NaDFOB can enhance the electrochemical performance in NaVO/Zn full cells.

3. Conclusion

In summary, we have investigated the EDL modification and the nucleation progress induced by the addition of NaDFOB in the $ZnSO_4$ electrolyte. It was illustrated that $DFOB^-$ replaced H_2O molecules in the EDL, minimizing water decomposition on the electrode surface. Meanwhile, the CA measurements and ex situ SEM results confirmed that the adsorption of $DFOB^-$ ions on the electrode resulted in progressive nucleation with nanoscale Zn nuclei, facilitating ultra-uniform Zn deposition. In contrast, the instantaneous nucleation in the additive-free $ZnSO_4$ electrolyte caused the formation of Zn dendrites. Moreover, the decomposition of adsorbed $DFOB^-$ yielded an inorganic SEI layer that effectively decreased the interfacial energy and regulated uniform Zn plating. As a consequence, the addition of $DFOB^-$ not only enabled highly reversible Zn plating/stripping behaviors with a CE of 99.3% in Zn/Cu half cells but also prompted a high capacity retention of 93.0% in NaVO/Zn full cells with a capacity of 250 mAh g^{-1}. This work provides new insights into the Zn nucleation and growth mechanism induced by the anion-modified EDL, facilitating the development of highly reversible and sustainable Zn electrodes for aqueous zinc-ion batteries.

Supporting Information

Supporting Information is available from the Wiley Online Library or from the author.

Acknowledgements

The authors gratefully acknowledge the Welch Foundation for their generous support through Grant No.'s F-1436 (C.B.M.) and F-1841 (G.H.). Z. W. also acknowledges the UT Austin Center for Electrochemistry (Welch Foundation grant H-F-0037) for providing a graduate research fellowship.

Conflict of Interest

The authors declare no conflict of interest.

Data Availability Statement

The data that support the findings of this study are available in the supplementary material of this article.

Keywords

electric double layer, nanoscale nuclei, progressive nucleation, solid electrolyte interphase, zinc-ion battery

Received: November 8, 2023
Revised: January 24, 2024
Published online: February 19, 2024

[1] B. Yong, D. Ma, Y. Wang, H. Mi, C. He, P. Zhang, *Adv. Energy Mater.* **2020**, *10*, 2002354.
[2] G. Fang, J. Zhou, A. Pan, S. Liang, *ACS Energy Lett.* **2018**, *3*, 2480.
[3] Y. Lv, Y. Xiao, L. Ma, C. Zhi, S. Chen, *Adv. Mater.* **2022**, *34*, 2106409.

[4] B. Tang, L. Shan, S. Liang, J. Zhou, *Energy Environ. Sci.* **2019**, *12*, 3288.
[5] X. Jia, C. Liu, Z. G. Neale, J. Yang, G. Cao, *Chem. Rev.* **2020**, *120*, 7795.
[6] Z. Liu, R. Wang, Q. Ma, J. Wan, S. Zhang, L. Zhang, H. Li, Q. Luo, J. Wu, T. Zhou, J. Mao, L. Zhang, C. Zhang, Z. Guo, *Adv. Funct. Mater.* **2023**, 2214538.
[7] J. Yang, H. Yan, H. Hao, Y. Song, Y. Li, Q. Liu, A. Tang, *ACS Energy Lett.* **2022**, *7*, 2331.
[8] L. Ding, L. Wang, J. Gao, T. Yan, H. Li, J. Mao, F. Song, S. Fedotov, L.-Y. Chang, N. Li, Y. Su, T. Liu, L. Zhang, *Adv. Funct. Mater.* **2023**, *33*, 2301648.
[9] H. J. Kim, S. Kim, K. Heo, J.-H. Lim, H. Yashiro, S.-T. Myung, *Adv. Energy Mater.* **2023**, *13*, 2203189.
[10] R. Chen, C. Zhang, J. Li, Z. Du, F. Guo, W. Zhang, Y. Dai, W. Zong, X. Gao, J. Zhu, Y. Zhao, X. Wang, G. He, *Energy Environ. Sci.* **2023**, *16*, 2540.
[11] X. Wang, Y. Ying, S. Chen, Q. Meng, H. Huang, L. Ma, *Nano Energy* **2024**, *119*, 109099.
[12] X. Xie, J. Li, Z. Xing, B. Lu, S. Liang, J. Zhou, *National Science Review* **2023**, *10*, nwac281.
[13] Y. Chen, F. Gong, W. Deng, H. Zhang, X. Wang, *Energy Storage Mater.* **2023**, *58*, 20.
[14] S. Tian, T. Hwang, Y. Tian, Y. Zhou, L. Zhou, T. Milazzo, S. Moon, S. Malakpour Estalaki, S. Wu, R. Jian, K. Balkus, T. Luo, K. Cho, G. Xiong, *ACS Nano* **2023**, *17*, 14930.
[15] X. Gao, H. Dong, C. J. Carmalt, G. He, *ChemElectroChem* **2023**, *10*, 202300200.
[16] X. Yang, H. Fan, F. Hu, S. Chen, K. Yan, L. Ma, *Nano-Micro Lett.* **2023**, *15*, 126.
[17] S. Chen, Y. Ying, L. Ma, D. Zhu, H. Huang, L. Song, C. Zhi, *Nat. Commun.* **2023**, *14*, 2925.
[18] N. Zhang, S. Huang, Z. Yuan, J. Zhu, Z. Zhao, Z. Niu, *Angew. Chem., Int. Ed.* **2021**, *60*, 2861.
[19] Y. Liu, Y. Li, X. Huang, H. Cao, Q. Zheng, Y. Huo, J. Zhao, D. Lin, B. Xu, *Small* **2022**, *18*, 2203061.
[20] Y. Wang, Y. Fan, D. Liao, Y. Wu, Y. Yu, C. Hu, *Energy Storage Mater.* **2022**, *51*, 212.
[21] R. Yi, X. Shi, Y. Tang, Y. Yang, P. Zhou, B. Lu, J. Zhou, *Small Structures* **2023**, *4*, 2300020.
[22] G. Zhang, X. Zhang, H. Liu, J. Li, Y. Chen, H. Duan, *Adv. Energy Mater.* **2021**, *11*, 2003927.
[23] Q. Zhang, J. Luan, X. Huang, L. Zhu, Y. Tang, X. Ji, H. Wang, *Small* **2020**, *16*, 2000929.
[24] L. Zeng, H. He, H. Chen, D. Luo, J. He, C. Zhang, *Adv. Energy Mater.* **2022**, *12*, 2103708.
[25] Y. An, Y. Tian, S. Xiong, J. Feng, Y. Qian, *ACS Nano* **2021**, *15*, 11828.
[26] Y. Fang, X. Xie, B. Zhang, Y. Chai, B. Lu, M. Liu, J. Zhou, S. Liang, *Adv. Funct. Mater.* **2022**, *32*, 2109671.
[27] C. Li, Z. Sun, T. Yang, L. Yu, N. Wei, Z. Tian, J. Cai, J. Lv, Y. Shao, M. H. Rümmeli, J. Sun, Z. Liu, *Adv. Mater.* **2020**, *32*, 2003425.
[28] Z. Hou, Y. Gao, H. Tan, B. Zhang, *Nat. Commun.* **2021**, *12*, 3083.
[29] Z. Li, C. Chen, R. Mi, W. Gan, J. Dai, M. Jiao, H. Xie, Y. Yao, S. Xiao, L. Hu, *Adv. Mater.* **2020**, *32*, 1906308.
[30] T. Wei, Y. Ren, Y. Wang, L. Mo, Z. Li, H. Zhang, L. Hu, G. Cao, *ACS Nano* **2023**, *17*, 3765.
[31] J. Wan, R. Wang, Z. Liu, L. Zhang, F. Liang, T. Zhou, S. Zhang, L. Zhang, Q. Lu, C. Zhang, Z. Guo, *ACS Nano* **2023**, *17*, 1610.
[32] D. Wang, Q. Li, Y. Zhao, H. Hong, H. Li, Z. Huang, G. Liang, Q. Yang, C. Zhi, *Adv. Energy Mater.* **2022**, *12*, 2102707.
[33] P. Sun, L. Ma, W. Zhou, M. Qiu, Z. Wang, D. Chao, W. Mai, *Angew. Chem., Int. Ed.* **2021**, *60*, 18247.
[34] Y. Xu, X. Zheng, J. Sun, W. Wang, M. Wang, Y. Yuan, M. Chuai, N. Chen, H. Hu, W. Chen, *Nano Lett.* **2022**, *22*, 3298.
[35] F. Zhao, Z. Jing, X. Guo, J. Li, H. Dong, Y. Tan, L. Liu, Y. Zhou, R. Owen, P. R. Shearing, D. J. L. Brett, G. He, I. P. Parkin, *Energy Storage Mater.* **2022**, *53*, 638.
[36] Y. Wang, L. Mo, X. Zhang, Y. Ren, T. Wei, Z. Li, Y. Huang, H. Zhang, G. Cao, L. Hu, *Adv. Energy Mater.* **2023**, *13*, 2301517.
[37] Y. Lin, Z. Mai, H. Liang, Y. Li, G. Yang, C. Wang, *Energy Environ. Sci.* **2023**, *16*, 687.
[38] D. Xie, Y. Sang, D.-H. Wang, W.-Y. Diao, F.-Y. Tao, C. Liu, J.-W. Wang, H.-Z. Sun, J.-P. Zhang, X.-L. Wu, *Angew. Chem., Int. Ed.* **2023**, *62*, 202216934.
[39] N. Wang, X. Chen, H. Wan, B. Zhang, K. Guan, J. Yao, J. Ji, J. Li, Y. Gan, L. Lv, L. Tao, G. Ma, H. Wang, J. Zhang, H. Wang, *Adv. Funct. Mater.* **2023**, *33*, 2300795.
[40] K. Yan, Y. Fan, F. Hu, G. Li, X. Yang, X. Wang, X. Li, C. Peng, W. Wang, H. Fan, L. Ma, *Adv. Funct. Mater.* **2023**, *34*, 2307740.
[41] D. Li, Y. Tang, S. Liang, B. Lu, G. Chen, J. Zhou, *Energy Environ. Sci.* **2023**, *16*, 3381.
[42] Q. Zhang, J. Luan, Y. Tang, X. Ji, H. Wang, *Angew. Chem., Int. Ed.* **2020**, *59*, 13180.
[43] J. Wu, *Chem. Rev.* **2022**, *122*, 10821.
[44] H. Helmholtz, *Ann. Phys.* **1853**, *165*, 353.
[45] D. C. Grahame, *Chem. Rev.* **1947**, *41*, 441.
[46] J. O. Bockris, M. A. V. Devanathan, K. Müller, *Proc. R. Soc. London, Ser. A* **1963**, *274*, 55.
[47] Y. Yang, H. Hua, Z. Lv, M. Zhang, C. Liu, Z. Wen, H. Xie, W. He, J. Zhao, C. C. Li, *Adv. Funct. Mater.* **2023**, *33*, 2212446.
[48] C. Huang, X. Zhao, S. Liu, Y. Hao, Q. Tang, A. Hu, Z. Liu, X. Chen, *Adv. Mater.* **2021**, *33*, 2100445.
[49] C. Yan, H.-R. Li, X. Chen, X.-Q. Zhang, X.-B. Cheng, R. Xu, J.-Q. Huang, Q. Zhang, *J. Am. Chem. Soc.* **2019**, *141*, 9422.
[50] Y. Zhong, Z. Cheng, H. Zhang, J. Li, D. Liu, Y. Liao, J. Meng, Y. Shen, Y. Huang, *Nano Energy* **2022**, *98*, 107220.
[51] F. Wan, Z. Niu, *Angew. Chem., Int. Ed.* **2019**, *58*, 16358.
[52] A. Pei, G. Zheng, F. Shi, Y. Li, Y. Cui, *Nano Lett.* **2017**, *17*, 1132.
[53] P. Biswal, S. Stalin, A. Kludze, S. Choudhury, L. A. Archer, *Nano Lett.* **2019**, *19*, 8191.
[54] M. Kim, J. Lee, Y. Kim, Y. Park, H. Kim, J. W. Choi, *J. Am. Chem. Soc.* **2023**, *145*, 15776.
[55] J. Li, Z. Liu, S. Han, P. Zhou, B. Lu, J. Zhou, Z. Zeng, Z. Chen, J. Zhou, *Nano-Micro Lett.* **2023**, *15*, 237.
[56] M. Liu, L. Yao, Y. Ji, M. Zhang, Y. Gan, Y. Cai, H. Li, W. Zhao, Y. Zhao, Z. Zou, R. Qin, Y. Wang, L. Liu, H. Liu, K. Yang, T. S. Miller, F. Pan, J. Yang, *Nano Lett.* **2023**, *23*, 541.
[57] M. Yang, J. Zhu, S. Bi, R. Wang, Z. Niu, *Adv. Mater.* **2022**, *34*, 2201744.
[58] J. Chen, Z. Huang, C. Wang, S. Porter, B. Wang, W. Lie, H. K. Liu, *Chem. Commun.* **2015**, *51*, 9809.
[59] H. Lu, X. Zhang, M. Luo, K. Cao, Y. Lu, B. B. Xu, H. Pan, K. Tao, Y. Jiang, *Adv. Funct. Mater.* **2021**, *31*, 2103514.
[60] Y. Li, P. Wu, W. Zhong, C. Xie, Y. Xie, Q. Zhang, D. Sun, Y. Tang, H. Wang, *Energy Environ. Sci.* **2021**, *14*, 5563.
[61] M. Liu, L. Yang, H. Liu, A. Amine, Q. Zhao, Y. Song, J. Yang, K. Wang, F. Pan, *ACS Appl. Mater. Interfaces* **2019**, *11*, 32046.
[62] K. Zhao, F. Liu, G. Fan, J. Liu, M. Yu, Z. Yan, N. Zhang, F. Cheng, *ACS Appl. Mater. Interfaces* **2021**, *13*, 47650.
[63] C. Huang, X. Zhao, Y. Hao, Y. Yang, Y. Qian, G. Chang, Y. Zhang, Q. Tang, A. Hu, X. Chen, *Adv. Funct. Mater.* **2022**, *32*, 2112091.
[64] Q. Wen, H. Fu, Z. Wang, Y. Huang, Z. He, C. Yan, J. Mao, K. Dai, X. Zhang, J. Zheng, *J. Mater. Chem. A* **2022**, *10*, 17501.
[65] M. Han, J. Huang, X. Xie, T. C. Li, J. Huang, S. Liang, J. Zhou, H. J. Fan, *Adv. Funct. Mater.* **2022**, *32*, 2110957.
[66] X. Xu, S. Li, H. Yan, J. Du, S. Yang, B. Li, *J. Energy Storage* **2023**, *72*, 108625.
[67] D. R. Ely, R. E. García, *J. Electrochem. Soc.* **2013**, *160*, A662.
[68] L. Makkonen, *J. Phys.: Condens. Matter* **2016**, *28*, 135001.
[69] D. Y. Kwok, D. Li, A. W. Neumann, *Colloids Surf. A* **1994**, *89*, 181.
[70] J. C. Ballesteros, P. Díaz-Arista, Y. Meas, R. Ortega, G. Trejo, *Electrochim. Acta* **2007**, *52*, 3686.

[71] X. Y. Liu, K. Maiwa, K. Tsukamoto, *J. Chem. Phys.* **1997**, *106*, 1870.
[72] M. Palomar-Pardavé, M. Miranda-Hernández, I. González, N. Batina, *Surf. Sci.* **1998**, *399*, 80.
[73] B. R. Scharifker, J. Mostany, *J. Electroanal. Chem. Interfacial Electrochem.* **1984**, *177*, 13.
[74] G. J. Hills, D. J. Schiffrin, J. Thompson, *Electrochim. Acta* **1974**, *19*, 657.
[75] J. Velmurugan, J.-M. Noël, W. Nogala, M. V. Mirkin, *Chem. Sci.* **2012**, *3*, 3307.
[76] G. Luo, Y. Yuan, D.-Y. Li, N. Li, G.-H. Yuan, *Coatings* **2022**, *12*, 1195.
[77] M. Sánchez Cruz, F. Alonso, J. M. Palacios, *J. Appl. Electrochem.* **1993**, *23*, 364.
[78] D. Anastasiadou, J. T. D. Janssen, E. J. M. Hensen, M. C. Figueiredo, *ChemElectroChem* **2023**, *10*, 202200842.
[79] J. Mostany, J. Mozota, B. R. Scharifker, *J. Electroanal. Chem. Interfacial Electrochem.* **1984**, *177*, 25.
[80] G. Trejo, H. Ruiz, R. O. Borges, Y. Meas, *J. Appl. Electrochem.* **2001**, *31*, 685.
[81] Z. Zhao, J. Zhao, Z. Hu, J. Li, J. Li, Y. Zhang, C. Wang, G. Cui, *Energy Environ. Sci.* **2019**, *12*, 1938.
[82] B. Scharifker, G. Hills, *Electrochim. Acta* **1983**, *28*, 879.
[83] G. J. Hills, D. J. Schiffrin, J. Thompson, *Electrochim. Acta* **1974**, *19*, 671.
[84] G. Trejo, R. Ortega B, Y. Meas, P. Ozil, E. Chainet, B. Nguyen, *J. Electrochem. Soc.* **1998**, *145*, 4090.
[85] K.-H. Chen, K. N. Wood, E. Kazyak, W. S. LePage, A. L. Davis, A. J. Sanchez, N. P. Dasgupta, *J. Mater. Chem. A* **2017**, *5*, 11671.
[86] C. Shin, L. Yao, S.-Y. Jeong, T. N. Ng, *Sci. Adv.* **2024**, *10*, eadf9951.
[87] J. Zhou, F. Wu, Y. Mei, Y. Hao, L. Li, M. Xie, R. Chen, *Adv. Mater.* **2022**, *34*, 2200782.
[88] X. Xie, S. Liang, J. Gao, S. Guo, J. Guo, C. Wang, G. Xu, X. Wu, G. Chen, J. Zhou, *Energy Environ. Sci.* **2020**, *13*, 503.
[89] P. Cao, X. Zhou, A. Wei, Q. Meng, H. Ye, W. Liu, J. Tang, J. Yang, *Adv. Funct. Mater.* **2021**, *31*, 2100398.
[90] F. Feng, D. O. Northwood, *Int. J. Hydrogen Energy* **2004**, *29*, 955.
[91] M. Abdallah, *Corros. Sci.* **2003**, *45*, 2705.
[92] J.-Y. Huot, *J. Electrochem. Soc.* **1989**, *136*, 1933.
[93] J. Perez, E. R. Gonzalez, H. M. Villullas, *J. Phys. Chem. B* **1998**, *102*, 10931.
[94] X. Huang, S. Yao, R. Zhou, X. Yang, X. Kan, J. Cheng, *J. Energy Storage* **2022**, *50*, 104246.
[95] Z. Wang, J. Diao, J. N. Burrow, K. K. Reimund, N. Katyal, G. Henkelman, C. B. Mullins, *Adv. Funct. Mater.* **2023**, 2304791.
[96] L. Gao, J. Chen, Q. Chen, X. Kong, *Sci. Adv.* **2022**, *8*, eabm4606.
[97] P. He, G. Zhang, X. Liao, M. Yan, X. Xu, Q. An, J. Liu, L. Mai, *Adv. Energy Mater.* **2018**, *8*, 1702463.
[98] Z. Wang, J. Diao, K. Kawashima, J. A. Weeks, R. R. Vaidyula, R. A. Marquez, N. Miller, G. Henkelman, C. B. Mullins, *J. Mater. Chem. A* **2023**, *11*, 18881.
[99] F. Wan, L. Zhang, X. Dai, X. Wang, Z. Niu, J. Chen, *Nat. Commun.* **2018**, *9*, 1656.

